

pubs.acs.org/acssensors Article

Delivering Robust Proton-Only Sensing of Hyperpolarized [1,2-¹³C₂]-Pyruvate Using Broad-Spectral-Range Nuclear Magnetic Resonance Pulse Sequences

Iuliia Mandzhieva, Isaiah Adelabu, Shiraz Nantogma, Eduard Y. Chekmenev,* and Thomas Theis*



Cite This: ACS Sens. 2023, 8, 4101-4110



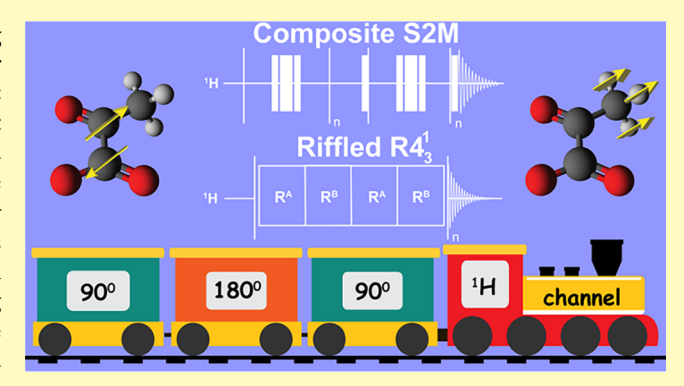
ACCESS I

III Metrics & More

Article Recommendations

s Supporting Information

ABSTRACT: Hyperpolarized [1-¹³C]pyruvate is the leading hyperpolarized injectable contrast agent and is currently under evaluation in clinical trials for molecular imaging of metabolic diseases, including cardiovascular disease and cancer. One aspect limiting broad scalability of the technique is that hyperpolarized ¹³C MRI requires specialized ¹³C hardware and software that are not generally available on clinical MRI scanners, which employ proton-only detection. Here, we present an approach that uses pulse sequences to transfer ¹³C hyperpolarization to methyl protons for detection of the ¹³C-¹³C pyruvate singlet, employing proton-only excitation and detection only. The new pulse sequences are robust to the B₁ and B₀ magnetic field inhomogeneities. The work focuses on singlet-to-magnetization



(S2M) and rotor-synchronized (R) pulses, both relying on trains of hard pulses with broad spectral width coverage designed to effectively transform hyperpolarized $^{13}C_2$ -singlet hyperpolarization to ^{1}H polarization on the CH₃ group of $[1,2^{-13}C_2]$ pyruvate. This approach may enable a broader adoption of hyperpolarized MRI as a molecular imaging technique.

KEYWORDS: parahydrogen, hyperpolarization, pyruvate, SABRE, proton sensing, molecular imaging

Modern hyperpolarization (HP) techniques enhance magnetic resonance (MR) signals by several orders of magnitude. The resulting enhancements overcome the inherent sensitivity limitations of MR technologies including nuclear magnetic resonance (NMR) spectroscopy and magnetic resonance imaging (MRI) and have enabled *in vivo* imaging of metabolic processes.

¹³C-labeled pyruvate is one of the most promising ¹³Chyperpolarized HP contrast agents because pyruvate plays a central role in mammalian metabolic cellular energy pathways. HP ¹³C-pyruvate can be used as biomarker for various diseases, such as cancer, ¹⁵ diabetes, ¹⁶ cardiovascular disease, ¹⁷ and neurological diseases. ¹⁸ The utility of HP ¹³C-pyruvate comes from the fact that ¹³C can retain the HP state for ~36 s, ¹ therefore allowing for sufficient amount of time to probe metabolic processes of pyruvate catabolism in vivo. Moreover, the ¹³C detection of HP ¹³C-labeled pyruvate offers a useful benefit of virtually no ¹³C background signal. Since clinical MRI scanners are narrowly focused around proton detection frequency, their electronics are not capable of ¹³C scanning. To circumvent this limitation, HP MRI of ¹³C-pyruvate is performed using specialized ¹³C capabilities of the MRI scanner (often referred to as multinuclear package) that can only be found on a few specialized research MRI scanners. Since the multinuclear scanner capability is not broadly available, there

remains a substantial translational challenge to enable HP ¹³Cpyruvate metabolic imaging on a wide range of already installed clinical scanners equipped with proton-only detection electronics. Moreover, the signal-to-noise ratio (SNR) is directly proportional to the Larmor frequency (SNR $\propto \omega_{\rm L}$)²⁰ of an inductive detector. The Larmor frequency (ω_L) of ¹H is roughly four times larger than that of ¹³C. In addition, the magnetic moment of the detected nucleus (¹H) is also four times larger, boosting the signal by another factor of 4. As a result, the detected signal on the ¹H channel can be up to 16 times larger under the assumption of 100% efficient polarization transfer. Losses due to imperfect polarization-transfer efficiency are considered in this paper accordingly. Previous examples of polarization transfer to ¹H for the detection of ¹³C hyperpolarization includes the use of INEPT, which still requires pulses on both ¹³C and ¹H channels. ²¹

Received: June 27, 2023
Revised: September 29, 2023
Accepted: October 24, 2023
Published: November 10, 2023





We have previously reported on a method for proton-only detection of overpopulated $^{13}C^{-13}C$ singlet state in $^{13}C_2$ -pyruvate. 22 This method employs a spin-lock-induced crossing (SLIC) RF excitation pulse applied to methyl to transfer polarization of the $^{13}C^{-13}C$ singlet state to methyl protons. 22 The key advantage of this approach is the requirement of proton-only scanner hardware to read the HP state stored by the $^{13}C^{-13}C$ singlet state in $[1,2^{-13}C_2]$ pyruvate. The key limitation of this approach is the requirement to create an overpopulated $^{13}C^{-13}C$ nuclear singlet state in $[1,2^{-13}C_2]$ pyruvate. However, it should be noted that SABRE hyperpolarization technique readily spontaneously enable creation of such singlet state in $[1,2^{-13}C_2]$ pyruvate. 23,24 Moreover, SABRE hyperpolarization technique has recently enjoyed a remarkable progress—indeed, the production and the in vivo utility of HP ^{13}C -labeled pyruvate via the SABRE technique has been recently demonstrated. $^{25-27}$

Despite the success of the pilot study, SLIC pulses require precise pulse calibration and highly homogeneous B_0 and B_1 fields. Here, we present a new proton-only detection method that is highly robust, even in the presence of pulse calibration errors and significant field inhomogeneities. This new protononly detection of the overpopulated ¹³C-¹³C nuclear singlet state in [1,2-¹³C₂]pyruvate employs singlet-to-magnetization (S2M) and rotor-synchronized (R) pulses, both relying on trains of hard RF pulses with broad spectral width coverage designed to effectively transform HP $^{13}\bar{C}_{2}\text{-singlet}$ hyperpolarization into ¹H polarization on the CH₃ group of [1,2-¹³C₂]pyruvate. The result of such proton excitation is the HP state of the methyl protons, which can be detected by standard ¹H RF coils. Moreover, when hyperpolarization is employed, high magnetic fields of costly superconducting magnets are no longer critical and lower-cost, low-field devices become almost equally sensitive. 1,7,10,15,28 Low magnetic fields are also important in the current demonstrations because the HP ¹³C₂-singlet state is naturally preserved at magnetic fields below 0.3 T and would require spin-locking at higher fields. Accordingly, in this article, we demonstrate robust HP pyruvate sensing using a low-field, 48.5 mT, MRI scanner only using the proton RF chain and pulse sequences without any ¹³C-related hardware or software. ²⁹ This approach has the potential to enable broader adoption of HP MRI as a molecular imaging technique.

In the presented experiments, the ¹³C₂ singlet state is hyperpolarized using the parahydrogen-based SABRE (Signal amplification by reversible exchange) approach, ^{4,23,24,30} albeit DNP methods could also be used. ^{31–34}

MATERIALS AND METHODS

Sample Preparation. The catalyst precursor [IrCl(COD)IMes] [COD = cyclooctadiene, IMes = 1,3-bis(2,4,6-trimethylphenyl)-imidazole-2-ylidene] was synthesized as described previously. $^{35-37}$ The sample contained 30 mM sodium [1,2- 13 C₂]pyruvate (Sigma-Aldrich-Isotec P/N 493392) as a substrate, 40 mM dimethyl sulfoxide as a coligand, and 6 mM catalyst precursor dissolved in methanol- 1 d₄. The samples were prepared by filling 0.6 mL of the stock solution into standard 5 mm NMR tubes (WG 1000–8, Wilmad), which were then flushed with argon for 1–2 min to remove oxygen and sealed under an argon atmosphere.

SABRE Hyperpolarization Setup. A schematic of the experimental setup is provided in Figure 1. Using this setup, we hyperpolarized sodium $[1,2^{-13}C_2]$ pyruvate by pressurizing the NMR tube to 8 bar total p-H₂ pressure for p-H₂ bubbling for 60 s with a flow rate set to 70 sccm at 1.7 μ T. As soon as the p-H₂ flow was turned off, the sample was transferred to 48.5 mT for detection (2-3 s time delay between

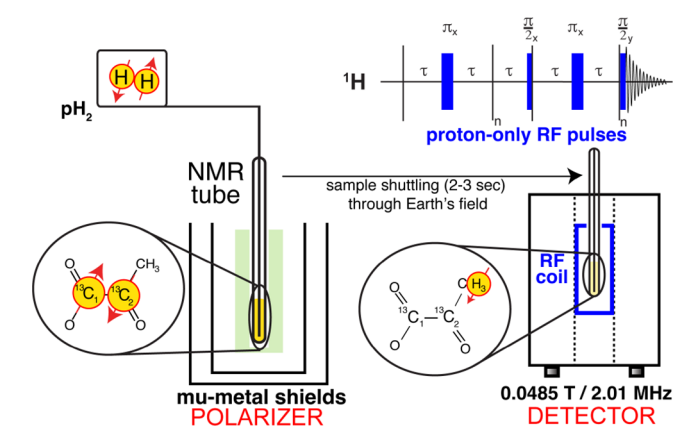


Figure 1. Experimental schematic for performing SABRE-SHEATH hyperpolarization followed by sample transfer and proton-only sensing of hyperpolarized [1,2-¹³C₂]pyruvate.

cessation of p-H $_2$ flow and initiation of polarization transfer sequence).

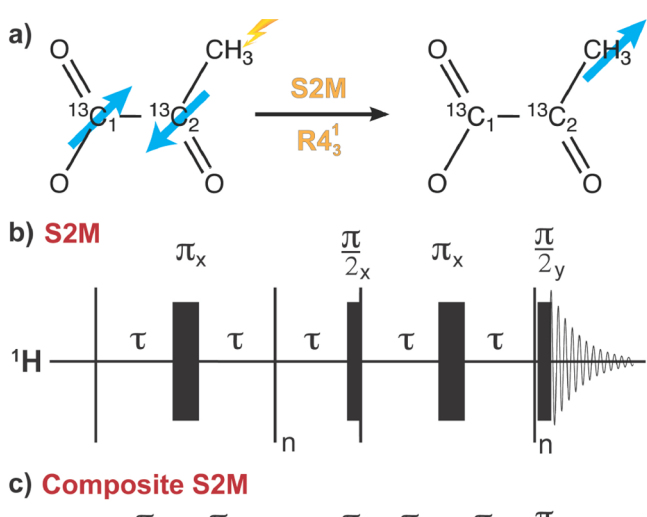
A p- H_2 generator, described elsewhere, ⁴⁰ was employed to produce 98.5% p- H_2 . A mass-flow controller (SmartTrak 50, Sierra Instruments) regulated the p- H_2 gas flow with the flow rate set to 70 standard cubic centimeters per minute (sccm). Parahydrogen was bubbled through the solution for catalyst activation ^{5,6} at 25 °C for 15 min before any experiments. During the catalyst activation period, the solution changed color from yellow to clear.

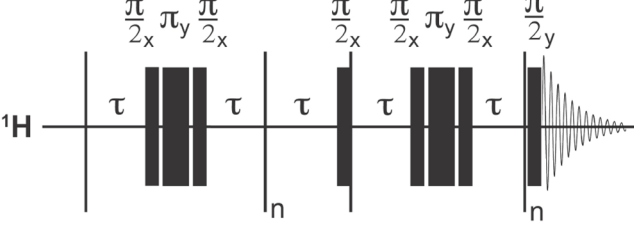
Hyperpolarization of $^{13}\text{C}-^{13}\text{C}$ Singlet State of [1,2- $^{13}\text{C}_2$]-Pyruvate. SABRE-SHEATH (signal amplification by reversible exchange-shield enables alignment transfer to heteronuclei) experiments were conducted in a μ -metal shield (3 layers, ZG-209, Magnetic Shield Corp). The degaussing circuitry employed here was described previously. The required magnetic field in the μ T regime is generated by a small solenoid coil inside the shield. 39,42

For detection at B_0 of 48.5 mT a permanent magnet-based system configured in a Halbach array was used (Magritek, Wellington, New Zealand).³⁸

For application of the RF excitation pulses, a RF multiturn solenoid coil was used on the $^1\mathrm{H}$ channel. 43 The NMR probe frequency was 2.01885 MHz. The S2M, composite S2M, and riffled R4 1_3 pulses were implemented using Magritek software.

Subsequently, as indicated in Figure 2a, three pulse sequences have been adopted to transfer the singlet hyperpolarization from the ¹³C₂ spin pair to the CH3 protons of pyruvate. Importantly, these pulse sequences are applied only to the CH₃ protons. As illustrated in Figures 2b–d, the employed pulse sequences are S2M, 44–47 composite S2M, 48 and riffled R4¹₃ pulses, ^{49–51} all applied only on the ¹H channel. The S2M pulse sequence involves two spin-echo trains separated by a 90° pulse (Figure 2b). Each echo train contains 180° pulses separated by a time delay of 27. The S2M pulse sequence generates z-magnetization on CH₃ protons; therefore, it is necessary to apply a 90° pulse after the S2M sequence to generate detectable, transverse xy-polarization. To increase the robustness of S2M against B_0 and B_1 inhomogeneities, it is useful to implement composite pulses within the sequence. Accordingly, the composite S2M pulse sequence (Figure 2c) uses compensated 180° rotations to ensure the high accuracy of the inversions required during the pulse train. The 180_x° pulses of S2M are replaced by composite $[90_x^{\circ}]$ $-180^{\circ}_{\nu} - 90^{\circ}_{x}$] pulses. An alternative to S2M approaches is rotorsynchronized (R) pulse trains. A good example is riffled R4¹ pulses, which are relatively new pulse sequences originally developed to implement electron-to-nuclear polarization transfer in diamond nitrogen-vacancy magnetometry, 49 which have recently been used for nuclear spin manipulations as well. 49 The riffled R4 1_3 name reflects the symmetry of the employed pulses, and as shown in Figure 2d, this pulse sequence consists of four blocks, RA-RB-RA-RB. The RA block consists of three hard pulses: 90° pulse with 135° phase, 180° pulse with 45° phase, and 90° pulse with 135° phase. The excitation RF pulses are separated





d) Riffled R4

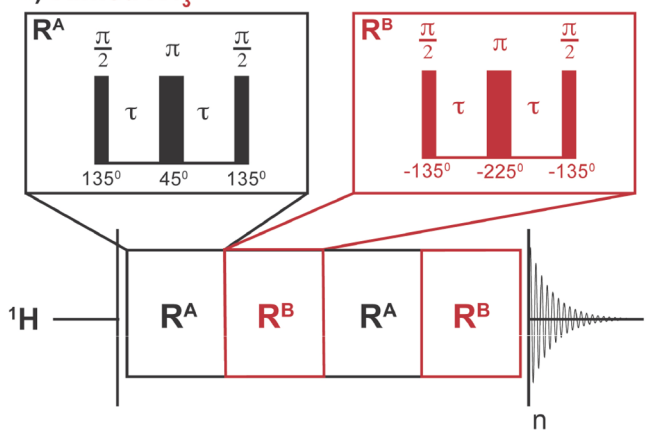


Figure 2. (a) Scheme of polarization transfer from the HP $^{13}C_1$ – $^{13}C_2$ singlet state of [1,2-13C₂]pyruvate to CH₃ group protons applying proton-only RF excitation pulses such as S2M or R4\frac{1}{3}. Corresponding schematic for the (b) S2M pulse scheme, (c) composite S2M pulse scheme, and (d) riffled R4¹ pulse scheme.

by the time delay, τ . The R^B block also consists of three hard pulses: 90° pulse with -135° phase, 180° pulse with a -225° phase, and 90° pulse with -135° phase. Pulses are separated by time delay, τ , and repeated ntimes. All the employed sequences can be expected to outperform the previous SLIC approach 22,52,53 in terms of tolerating B_0 and B_1 inhomogeneities as experimentally and theoretically explored in this

Numerical Simulation. Simulations matching the experiments were performed using SPINACH⁵⁴ simulation library version 2.6.5625 in MATLAB (R2021a) as detailed in the Supporting Information.

RESULTS AND DISCUSSION

To explore and test the performance of S2M, composite S2M, and riffled R4¹ pulse sequences, we first simulated the effects of varying pulse sequence parameters within these sequences to assert their ability to deliver the desired ¹³C₂ to ¹H polarization

transfer. For all the sequences, the most critical parameters are the time-delay between pulses τ and the number of pulses n. The simulations were performed on the 5-spin [1,2-13C₂]pyruvate system $(^{13}C_1, ^{13}C_2, ^{-})$ and three protons on the CH₃ group).

Figure 3a shows a simulated 3D plot on how generated ¹Hmagnetization on the CH_3 group depends on time delay, τ , and number of cycles, n, after S2M. All simulations in Figure 3 are identical for S2M and composite S2M because the simulations assume perfect 180° pulses for either sequence. In experiments that suffer from B_1 and B_0 inhomogeneities, significant differences can be expected between S2M and composite S2M because the $[90^{\circ}_{x} - 180^{\circ}_{y} - 90^{\circ}_{x}]$ pulses are designed to compensate for errors accrued during single 180° pulse used in S2M. Figure 3b,e shows projections of the simulated 3D plot at constant n and constant τ , respectively.

Experimentally, complete multidimensional explorations are not realistic because of the large number of required tests; thus, guided by the simulations, we first ran a τ sweep, followed by nsweep to find the optimal settings. For the τ sweep, we used a fixed value of the number of cycles (n = 17) and presented the results plotted in Figure 3c for S2M and in Figure 3d for composite S2M. Generally, the τ sweep experimental data is in good agreement with the simulation shown in Figures 3b. A relatively sharp dependence on τ is observed in all cases with a maximum at $\tau = 3.97$ ms. Optimal values for τ obtained in simulations and experiment is in good agreement with the theatrically predicted value of τ of 4.01 ms⁴⁵ according to

$$\tau = \frac{1}{4(\sqrt{J_{\text{CC}}^2 + \Delta J_{\text{CH}}^2 + \Delta \omega_{\text{CC}}^2})}$$
$$= \frac{1}{4(\sqrt{60^2 + 6.38^2 + 15.57^2})}$$
$$\approx 4.01 \text{ms}$$

Comparing the experimental S2M and composite S2M results, the composite S2M produces significantly higher polarization (almost 2-fold) and the match with simulation is better. This result clearly indicates the importance of including composite pulses when B_1 and B_0 inhomogeneities or miscalibrations are present.

After optimizing τ to 3.97 ms, we used this value to run the subsequent *n* sweep shown in Figures 3e–g. Figure 3e shows the simulation for the S2M n sweep revealing a periodic behavior with maxima at $n \approx 17$ and $n \approx 48$ without polarization losses. In contrast, the experimental data Figures 3 f,g shows two peaks; the first at $n \approx 17$, in agreement with simulation, however, followed by a much smaller maximum at $n \approx 58$. The mismatch between simulation and experiment can be explained by T_1 and T_2 relaxation occurring in the experiment, which is not included in the simulation. Another important factor is that the S2M pulse sequence is very sensitive to inaccuracies in the pulse calibrations. This also may explain why the second maximum is larger for composite S2M that compensates for imperfections in the pulses.

In addition to S2M, and composite S2M pulse sequences, we implemented the Riffled rotor-synchronized $R4_3^{\Gamma}$ pulse sequence. Figure 4 shows a simulation of the $^{13}C_2$ to ^{1}H polarization transfer as a function of n and τ for this pulse sequence. Figure 4b,d shows projections out of the 3D plot for constant τ , and a constant number of cycles, n, respectively. As discussed above, for the experiments, a full 3D exploration is unreasonable, and we took a slice from the 3D plot to get a τ

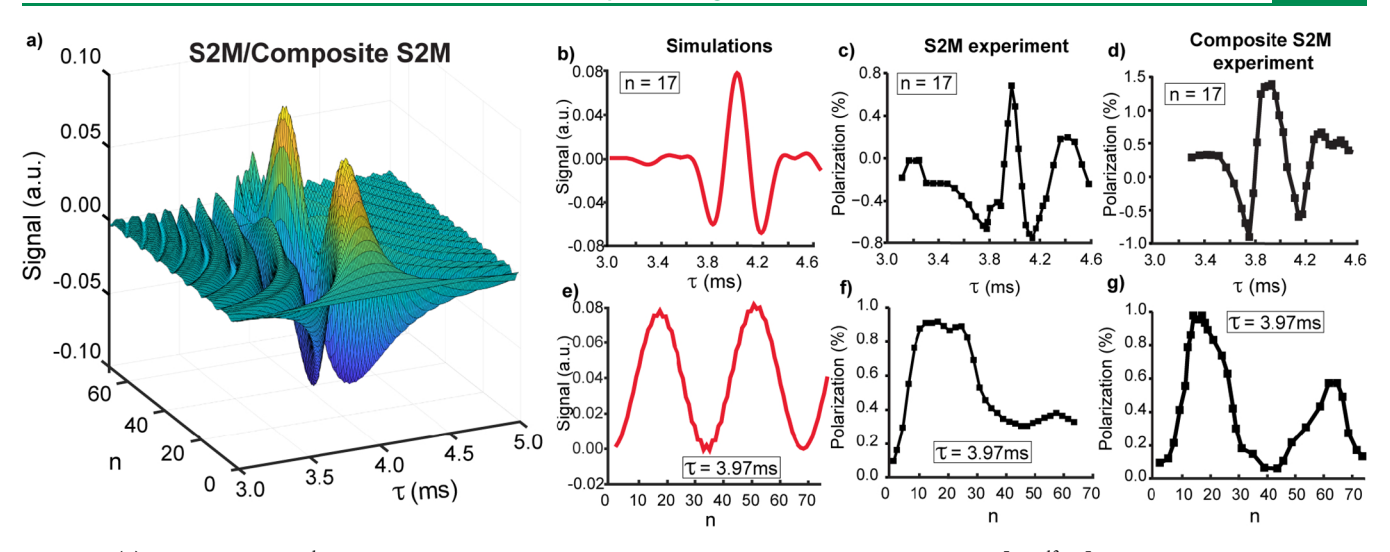


Figure 3. (a) 3D simulation of 1 H magnetization after application of a S2M/composite-S2M pulses to HP $[1,2^{-13}C_2]$ pyruvate as a function of time delay, τ , and number of cycles, n. (b) Simulated τ sweep acquired after S2M/composite-S2M pulse with n=17. (c) Experimental τ sweep acquired after S2M pulse with n=17 and 2.01885 MHz frequency. (d) Experimental τ sweep acquired after composite-S2M pulse with n=17 and 2.01885 MHz frequency. (e) Simulated n sweep acquired after S2M/composite-S2M pulse with $\tau=3.97$ ms. (f) Experimental n sweep acquired after S2M pulse with $\tau=3.97$ ms and 2.01885 MHz frequency. (g) Experimental n sweep acquired after S2M pulse with $\tau=3.97$ ms and 2.01885 MHz frequency.

sweep with fixed number of the riffled $R4_3^1$ cycle sequence (n=5). The experimental data (Figure 4c) is in good agreement with the simulation (Figure 4b). The maximum value of polarization was reached at $\tau=5.95$ ms. We used this value to optimize the number of cycles n. Figure 4d,e shows simulated and experimental data for an n sweep of the riffled $R4_3^1$ sequence. The experimental data follow the simulated trend for the first peak at n=5; however, the second simulated peak at n=12 is less pronounced for the experimental plot. The mismatch between simulation and experiment for the second peak likely arises because we do not take relaxation into account in the simulations. In addition, as shown in Figure 2d, Riffled $R4_3^1$ pulses contain four blocks with hard 90 and 180° pulses, making the duration of the whole pulse sequence almost twice as long as that of the composite S2M.

In order to gain a deeper understanding of the hyperpolarization transfer mechanism and the involved quantum states, we can trace the density matrix as a function of time during the polarization transfer sequences. For simplicity we consider three-spin system ${}^{13}C_1$, ${}^{13}C_2$ and ${}^{1}H$ for $[1,2^{-13}C_2]$ pyruvate (here, we model the three methyl group protons as one single proton). Further, we switch to the singlet-triplet based basis set (STZ) associated with states: S_0 , T_0 , T_- , and T_+ for $^{13}\text{C}_2$ -singlet and α or β states for ^{1}H . There are eight possible states for this system $|S_0\alpha\rangle$, $|T_0\alpha\rangle$, $|T_-\alpha\rangle$, $|T_+\alpha\rangle$, $|S_0\beta\rangle$, $|T_0\beta\rangle$, $|T_0\beta\rangle$ $T_{-}\beta$ >, and $|T_{+}\beta$ >. The main goal of the manuscript is to transfer polarization from the S₀ state of the carbon singlet to ¹Hmagnetization. In computer simulations, we can monitor matrix overlap between the density matrix of the spin system and state of the interest (for example, S_0). Analogously, we can monitor matrix overlap between the current density matrix and ¹H magnetization (I_{\sim}) .

Under optimal conditions for S2M/Composite S2M (τ = 3.97 ms and n = 17), we can monitor how the carbon singlet state is first converted to carbon- T_0 and subsequently to ${}^1\text{H}$ -magnetization. As shown on Figure 5a—d, the polarization travels from the $|S_0\alpha\rangle$ state to $|T_0\alpha\rangle$ and eventually to $|T_0\beta\rangle$ under application of S2M/compositeS2M pulses as a function of loop index. At loop #17, the population of S_0 reaches its minimal

values, while the population of T_0 reaches its maximum; both S_0 and T_0 plateau after loop #17. At the same time, ¹H-magnetization demonstrates a steady rise after loop #17. At the end of the pulse sequence, ¹H-magnetization reaches its maximum.

Similarly, on Figure 5e—h, we can monitor the density matrix during the riffled R4 $_3^1$ pulse sequence under its optimal conditions ($\tau = 5.95$ ms and n = 5). Interestingly, the 1 H-magnetization plot does not have a "threshold"; we can see polarization transfer from S_0 to T_0 ; and 1 H is created with the first series of riffled R4 $_3^1$ pulses (the first loop). The S_0 plot declines quickly, and at the same time, the T_0 and 1 H plot rise with the same slope. Detailed theory for these pulse sequences is found in ref 49 for riffled R4 $_3^1$ and in refs 46,55 for S2M.

Figure 6 examines the effect of B_1 inhomogeneities and pulse miscalibrations. For this study, we varied the pulse angle, α , in both simulations and experiments to examine how robust the polarization transfer is under varying B_1 power.

First, for the S2M pulse sequence, the simulations (Figure 6a) and experiments (Figure 6b) show that the S2M pulse sequence without composite pulses is very sensitive to pulse miscalibrations and B_1 inhomogeneities because small variations in the tip angle make the polarization transfer inefficient. Figure 6a demonstrates that a change in tip angle by a few degrees quickly affects the signal level. This is substantiated by the experimental plot (Figure 6b), showing that deviations from a 90° pulse of only ±3° cause a significant decay in polarization transfer efficiency. To mitigate the effect of miscalibrations and B_1 inhomogeneities, the composite-S2M pulse sequence was designed and tested. Figure 6c shows simulations of the polarization transfer efficiency for the composite-S2M pulse sequence. Compared to the S2M sequence, the simulated composite-S2M sequence demonstrates a higher level of robustness against miscalibration. There are no oscillations within the 80–100° range. The experimental plot (Figure 6d) also demonstrates improved pulse-miscalibration robustness in comparison to that of S2M. Acceptable values for the tip-angle for composite-S2M are within an $\pm 10^{\circ}$ range. Finally, we tested the riffled R43 pulse sequence for robustness to tip-angle

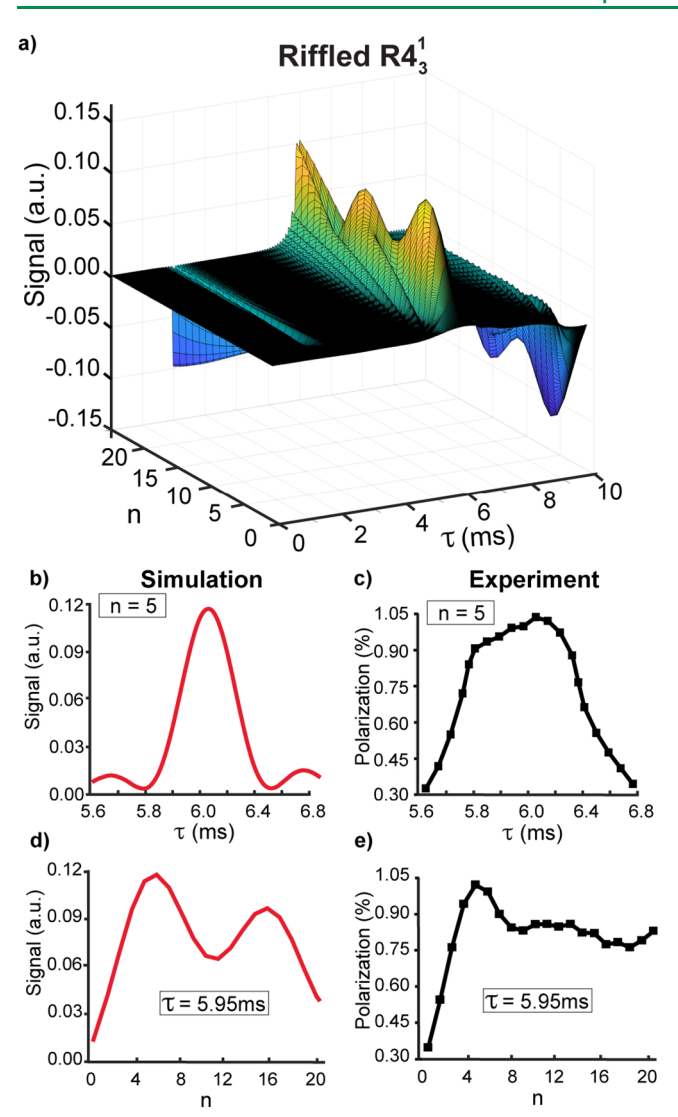


Figure 4. (a) 3D simulation of 1H generated magnetization after application of riffled R4 $_3^1$ pulses to HP $[1,2^{-13}C_2]$ pyruvate as a function of time delay, τ , and number of cycles, n. (b) Simulated τ sweep acquired after riffled R4 $_3^1$ pulses with n=5. (c) Experimental τ sweep acquired after riffled R4 $_3^1$ pulses with n=5 and with 2.01885 MHz frequency. (d) Simulated n sweep acquired after riffled R4 $_3^1$ pulses with $\tau=5.95$ ms. (e) Experimental n sweep acquired after $\pi=5.95$ ms and 2.01885 MHz frequency.

miscalibrations and B_1 inhomogeneities in both simulations (Figure 6e) and experiments (Figure 6f). The riffled R4 $_3^1$ pulse sequence shows robustness over an exceptionally wide range of pulse angles. Similar, to the composite-S2M, there are no oscillations for simulated polarization transfer-efficiency under the riffled R4 $_3^1$ pulse sequence (Figure 6e). These simulations show that it is possible to reach signal values over half of the maximum within the pulse-angle range from 60 to120°. The experimental data for the riffled R4 $_3^1$ pulse sequence (Figure 6f) validate the simulated results, showing that signal values above the half-maximum are obtained within the pulse angle range from 65 to 110°.

Since we did not incorporate any relaxation effects and B_0 inhomogeneity in our model for simulations, the experimental and simulated data are not in perfect agreement.

Another important parameter for proton-only sensing is the response to B_0 inhomogeneity. We explored this issue by varying

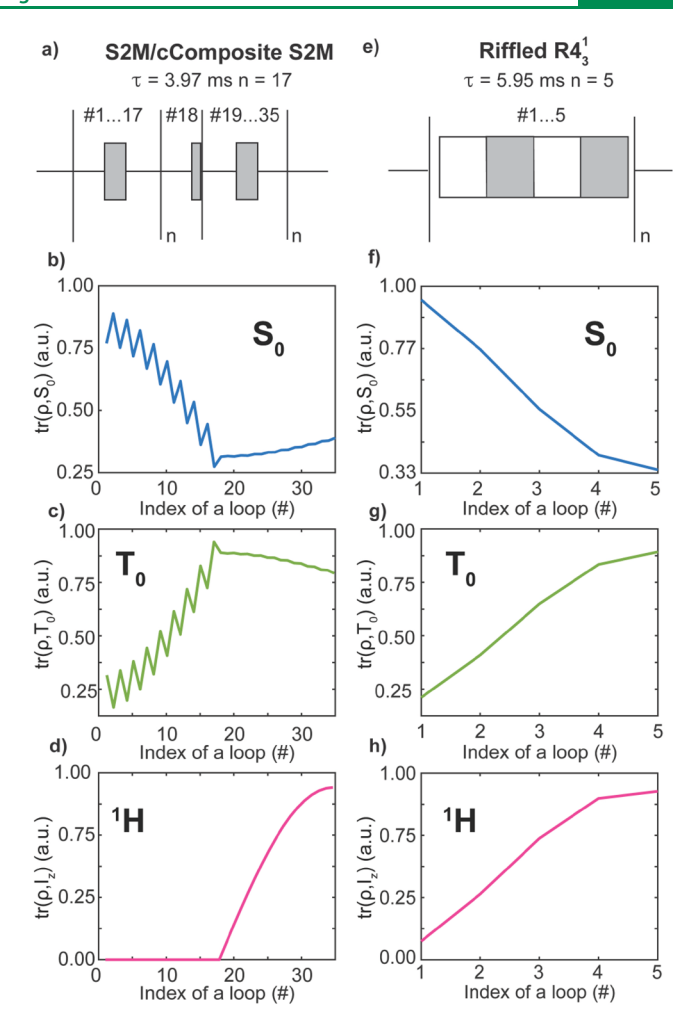


Figure 5. (a) S2M/composite S2M pulse scheme. Matrix overlap between the density matrix of the three-spin system of $[1,2^{-13}C_2]$ -pyruvate and (b) S_0 , (c) T_0 , and (d) 1 H-magnetization (I_z) as a function of loop index for S2M/composite S2M pulses. (e) Riffled R4 $_3^1$ pulse scheme. Matrix overlap between the density matrix of the three-spin system of $[1,2^{-13}C_2]$ pyruvate and (f) S_0 , (g) T_0 , and (h) 1 H-magnetization (I_z) for riffled R4 $_3^1$ pulses. Optimum conditions applied for S2M/composite S2M: $\tau = 3.97$ ms and n = 17; for riffled R4 $_3^1$: $\tau = 5.95$ ms and n = 5.

the B_1 frequency offset (as opposed to the B_1 power varied above). By experimentally changing the frequency offset, we can quantify the robustness to B_0 inhomogeneity. Here, we did not perform simulations because in the simulations employed above, all pulses were simulated as instantaneous events. To examine frequency offset changes by simulation would require simulations of effects during pulse application, which is beyond the scope of this manuscript.

Figure 7a–c examines the sensitivity of S2M, composite S2M, and riffled R4 $_3^1$ pulse sequences to the B_1 frequency offset, Ω , and compares the results to a ramped SLIC pulse that we reported recently. We find that all our new pulse sequences used in this paper significantly outperform ramped SLIC. Specifically, S2M can operate well within a comparatively narrower range of -750 to +300 Hz (Figure 7a), whereas composite S2M can operate within a very wide range of frequency offset from -1500 to +1500 Hz (Figure 7b). The riffled R4 $_3^1$ is suitable for a -1000 to 1000 Hz frequency rage (Figure 7c). In contrast, Ramped SLIC pulse is operational within a range of -200 to 200 Hz of Ω (Figure 7d).

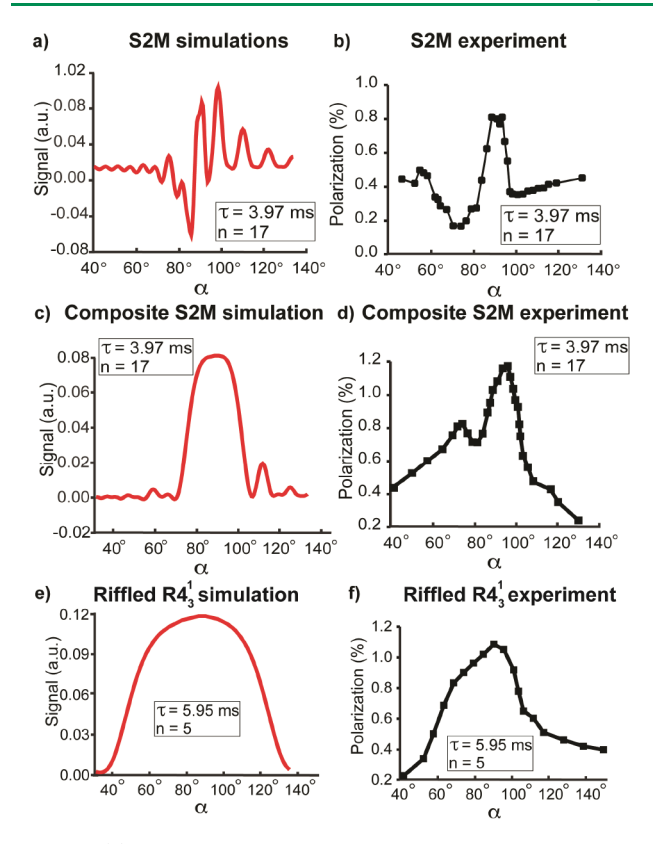


Figure 6. (a) Simulated 90° angle sweep acquired after S2M pulse with $\tau=3.97$ and n=17. α is angle of the applied RF pulse. (b) Experimental 900 angle sweep acquired after S2M pulse with $\tau=3.97$ and n=17. (c) Simulated 900 angle sweep acquired after composite S2M pulse with $\tau=3.97$ and n=17. (d) Experimental 90° angle sweep acquired after composite S2M pulse with $\tau=3.97$ and n=17 (e) Simulated 90° angle sweep acquired after riffled $R4_3^1$ pulses with $\tau=5.95$ ms and n=5. (f) Experimental 90° angle sweep acquired after riffled $R4_3^1$ pulses with $\tau=5.95$ ms and n=5.

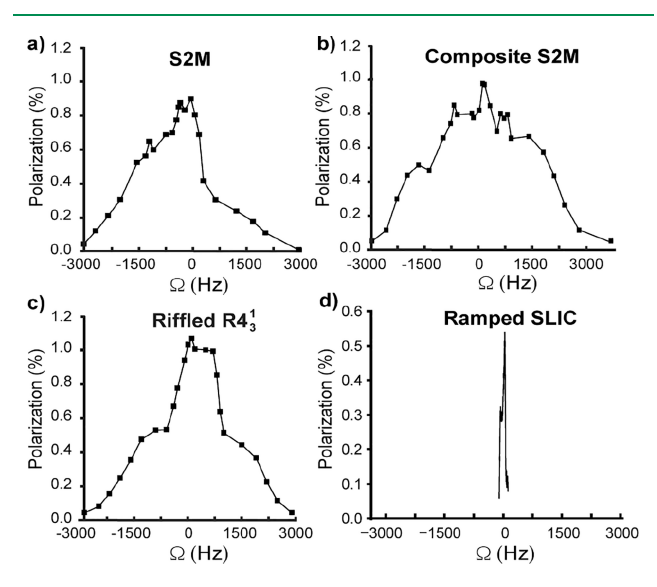


Figure 7. (a) Frequency offset sweep acquired after S2M pulses with $\tau = 3.97$ ms and n = 17. (b) Frequency offset sweep acquired after composite S2M pulses with $\tau = 3.97$ ms and n = 17. (c) Frequency offset sweep acquired after riffled R4 $_3^1$ pulses with $\tau = 5.95$ ms and n = 5. (d) Frequency offset sweep acquired after ramped SLIC pulses with $B_1 = 684$ Hz and a pulse duration of 1 s.

The efficiency of polarization transfer depends on not only the fundamental symmetry limitations of this problem but also the relative length of T_2 compared to the duration of the polarization transfer sequences. The S2M scheme uses $\tau=3.97$ ms and n=17, such that the total pulse scheme duration for S2M is 3.97 ms \times 17 \times 2 \times 2 + 3.97 ms = 273.93 ms \approx 0.274 s. The S2M composite has almost an identical duration, and the R4 1_3 scheme uses $\tau=5.95$ ms and n=5, such that the total pulse scheme duration for R4 1_3 is 5.95 ms \times 2 \times 4 \times 5 = 238 ms = 0.238 s. We estimate the T_2 values to be about 1 order of magnitude larger than the polarization transfer sequences. Based on the comparison of our numerical simulations with the experimental findings, the T_2 losses during the polarization transfer sequences are minimal.

After injection of hyperpolarized pyruvate, metabolic conversion to lactate can often be observed, which is particularly pronounced in tumors. 7,14,56

So, to illustrate future application and the ability to distinguish pyruvate from lactate even at low fields using the presented pulse sequences, first, we need to consider both $[1,2^{-13}C_2]$ pyruvate and $[1,2^{-13}C_2]$ lactate spin systems. Pyruvate has five spins, which consist of two carbons and three protons on the methyl group. Since all methyl group protons are equivalent, we may simplify it to a three-spin system: two carbons and one methyl group proton. Lactate has six NMR active spins. Similar to pyruvate, lactate has two carbons and three protons on the methyl group; however, it also has a proton attached to the $2^{-13}C$ site. Analogously to pyruvate case, we simplify it to a 4-spin system: two carbons, one proton at $2^{-13}C$ site, and one methyl group proton. All J coupling values are presented in the Supporting Information.

At a 48.6 mT magnetic field, singlet and triplet states of pyruvate are eigenstates of the Hamiltonian, which leads to a long-lived singlet state once formed. The long-lived pyruvate singlet state ($T_s \approx 40~\rm s$) can be used to store hyperpolarization during injections in vivo studies. After injection and conversion to lactate, the *J*-couplings between 2- 13 C and 1 H is larger than the *J*-coupling between 1- 13 C and 2- 13 C. $J(2-^{13}C-^{1}H)=140.0$ Hz, whereas $J(1-^{13}C-2-^{13}C)=43.6$ Hz. We can take advantage of this change in the *J*-coupling network to distinguish pyruvate from lactate, and we propose the following scheme of experiments applied on the 1 H channel alone as simulated and displayed in Figure 8.

For the S2M sequences,

- We first apply the S2M/composite S2M pulse sequence with n=2 and $\tau=3.5$ ms, which are the optimal parameters for the detection of lactate. When this sequence is executed, the singlet state that exists on the remaining pyruvate pool is unaffected (see Figure 8a).
- Thereafter, we can apply the S2M/composite S2M pulse sequence with n = 17 and $\tau = 3.97$ ms parameters optimal for the detection of pyruvate (note that the lactate signal is almost zero, Figure 8b).

With this procedure, separate detection of pyruvate and its metabolic product, lactate, can be accomplished.

Analogously, for the riffled R4¹ pulse sequence,

We first apply the riffled R4 $_3^1$ pulse sequence with n=1 and $\tau=6.3$ ms, which are the optimal parameters for lactate detection. Again, the pyruvate singlet remains unaffected (see Figure 8c).

Then, we apply the riffled R4 $_3^1$ pulse sequence with n = 5 and $\tau = 9.91$ ms, which are the optimal parameters for

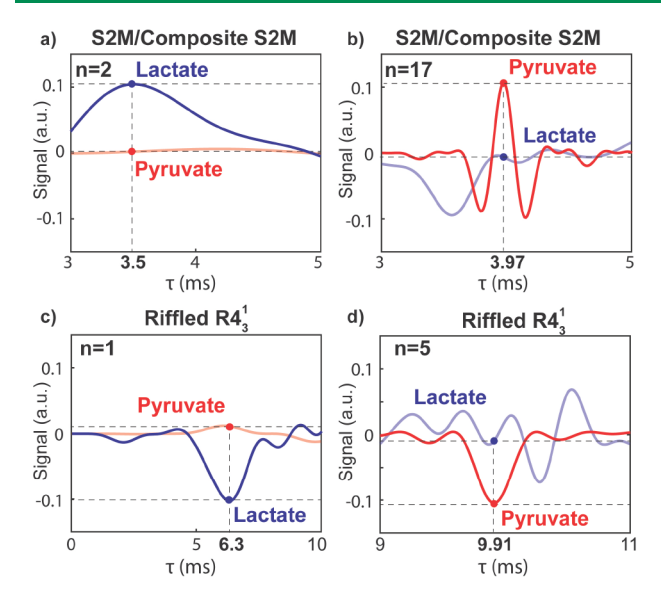


Figure 8. Computer simulations used to demonstrate the possibility to separate pyruvate from lactate by applying different sets of optimum parameters before detection to read our signals from different molecules. S2M/composite S2M pulse sequence: (a) Lactate detection regime (optimum parameters: n=2 and $\tau=3.5$ ms). The signal from lactate is at its maximum, whereas the pyruvate signal is almost zero. (b) Pyruvate detection regime (optimum parameters: n=17 and $\tau=3.97$ ms). The signal from pyruvate is at its maximum, whereas the lactate signal is almost zero. Riffled R4 $_3^1$ pulse sequence: (c) lactate detection regime (optimum parameters: n=1 and $\tau=6.3$ ms). The signal from lactate is at its maximum, whereas the pyruvate signal is almost zero. (d) Pyruvate detection regime (optimum parameters: n=5 and $\tau=9.91$ ms). The signal from pyruvate is at its maximum, whereas the lactate signal is almost zero.

detection of pyruvate (note that the lactate signal is almost zero, Figure 8d).

CONCLUSIONS

In summary, we present a robust proton-only low-field MR method to transfer polarization from the hyperpolarized $^{13}\mathrm{C}-^{13}\mathrm{C}$ -singlet state of [1,2- $^{13}\mathrm{C}_2$]pyruvate to methyl group protons for highly sensitive detection. S2M, composite S2M, and riffled $R4_3^1$ pulses demonstrated that polarization transfer is successful even in the presence of significant pulse calibration errors (B_1 inhomogeneities) and B_1 frequency offsets (corresponding to B_0 inhomogeneities). The experimentally estimated efficiency of polarization transfer by S2M is ~25%, that by composite S2M is ~38%, and that by riffled $R4_3^1$ is ~31%.

This work was inspired by the shortcomings of the previously employed SLIC pulses, which use long, soft pulses that are susceptible to B_1 and B_0 inhomogeneities. Here, we explored more advanced pulse sequences that employ trains of hard pulses instead. First, we explored the use of S2M sequence and found it to be highly efficient for proton-only sensing under optimized conditions; however, we found S2M to be highly susceptible to pulse-calibration errors. Therefore, we integrated composite $90^{\circ}-180^{\circ}-90^{\circ}$ pulses into S2M to generate the composite S2M pulse sequence to further mitigate artifacts due to B_0 and B_1 inhomogeneities. We found that the composite S2M generally outperforms the regular S2M pulse sequence in terms of polarization transfer efficiency, in some cases producing up to twice as much proton signal/polarization. Finally, we tested a relatively new rotor-synchronized pulse sequence, riffled

R4 $_3^1$. The riffled R4 $_3^1$ sequence demonstrated great robustness against pulse calibration errors and stability over a wide range of pulse angles in both simulation and experiment. In contrast to SLIC experiments, S2M, composite S2M, and riffled R4 $_3^1$ pulses are highly effective for proton-only sensing, even in the presence of significant B_1 inhomogeneities and several kHz in frequency offsets. Composite S2M works reliably over ~2 kHz frequency offset (vs riffled R4 $_3^1$ over ~1 kHz), whereas the riffled R4 $_3^1$ sequence works reliably over a large ~ $\pm 25^{\circ}$ B_1 error (vs composite S2M over $\pm 10^{\circ}$).

In addition, computer simulations predicted the possibility to distinguish $[1,2^{-13}C_2]$ pyruvate and its metabolic product $[1,2^{-13}C_2]$ lactate in vivo studies by applying broad-band pulses with various optimal parameters.

Overall, proton-only sensing with these new pulse sequences allows for the detection of $^{13}C-^{13}C$ hyperpolarization with low-field MRI scanners that only have ^{1}H channels. The novel pulse sequences address the challenges associated with such systems residing in B_0 and B_1 inhomogeneities.

ASSOCIATED CONTENT

Solution Supporting Information

The Supporting Information is available free of charge at https://pubs.acs.org/doi/10.1021/acssensors.3c01296.

MATLAB code used in simulations, magnetic field sweeps, and polarization calculations (PDF)

AUTHOR INFORMATION

Corresponding Authors

Eduard Y. Chekmenev — Department of Chemistry and Biosciences (Ibio), Wayne State University, Detroit, Michigan 48202, United States; Karmanos Cancer Institute (KCI), Detroit, Michigan 48201, United States; orcid.org/0000-0002-8745-8801; Email: chekmenevlab@gmail.com

Thomas Theis — Department of Chemistry and Department of Physics, North Carolina State University, Raleigh, North Carolina 27606, United States; Joint Department of Biomedical Engineering, University of North Carolina at Chapel Hill and North Carolina State University, Raleigh, North Carolina 27695, United States; orcid.org/0000-0001-6779-9978; Email: ttheis@ncsu.edu

Authors

Iuliia Mandzhieva — Department of Chemistry, North Carolina State University, Raleigh, North Carolina 27606, United States; Occid.org/0000-0001-9154-9012

Isaiah Adelabu — Department of Chemistry, Wayne State University, Detroit, Michigan 48202, United States; orcid.org/0000-0002-9475-0851

Shiraz Nantogma – Department of Chemistry, Wayne State University, Detroit, Michigan 48202, United States

Complete contact information is available at: https://pubs.acs.org/10.1021/acssensors.3c01296

Notes

The authors declare the following competing financial interest(s): Thomas Theis holds stock in Vizma Life Sciences LLC (VLS) and is President of VLS. VLS is developing products related to the research being reported. The terms of this arrangement have been reviewed and approved by NC State University in accordance with its policy on objectivity in research. The authors have filed a provisional patent application

through NC State University with the USPTO regarding this work (Application no. 63/203,591). Euard Y. Chekmenev discloses a stake of ownership in XeUS Technologies, Ltd., and VLS.

ACKNOWLEDGMENTS

Research reported in this publication was supported by the National Institute of Biomedical Imaging and Bioengineering of the National Institutes of Health under award nos. NIH R21EB025313, NIH R01EB029829, and R21EB033872. The content is solely the responsibility of the authors and does not necessarily represent the official views of the National Institutes of Health. In addition, we acknowledge funding from the Mallinckrodt Foundation, the National Science Foundation under award no. NSF CHE-1904780, the North Carolina Biotechnology Center in the form of a Translational Research Grant, and WSU Thomas C. Rumble University Graduate Fellowship (I.A. and S.N.). Finally, we would like to acknowledge the support from NCSU's METRIC providing access to NMR instrumentation. This material is based upon work supported by the U.S. Department of Energy, Office of Biological and Environmental Research (BER) under award number(s) DE-SC0023334. Disclaimer: "This report was prepared as an account of work sponsored by an agency of the United States Government. Neither the United States Government nor any agency thereof, nor any of their employees, makes any warranty, express or implied, or assumes any legal liability or responsibility for the accuracy, completeness, or usefulness of any information, apparatus, product, or process disclosed, or represents that its use would not infringe privately owned rights. Reference herein to any specific commercial product, process, or service by trade name, trademark, manufacturer, or otherwise does not necessarily constitute or imply its endorsement, recommendation, or favoring by the United States Government or any agency thereof. The views and opinions of authors expressed herein do not necessarily state or reflect those of the United States Government or any agency.

ABBREVIATIONS

HP, hyperpolarization; SLIC, spin-lock-induced crossing; S2M, singlet-to-magnetization

■ REFERENCES

- (1) Eills, J.; Budker, D.; Cavagnero, S.; Chekmenev, E. Y.; Elliott, S. J.; Jannin, S.; Lesage, A.; Matysik, J.; Meersmann, T.; Prisner, T.; Reimer, J. A.; Yang, H.; Koptyug, I. V. Spin Hyperpolarization in Modern Magnetic Resonance. *Chem. Rev.* **2023**. *12*31417.
- (2) Truong, M. L.; Theis, T.; Coffey, A. M.; Shchepin, R. V.; Waddell, K. W.; Shi, F.; Goodson, B. M.; Warren, W. S.; Chekmenev, E. Y. ¹⁵N Hyperpolarization by Reversible Exchange Using SABRE-SHEATH. *J. Phys. Chem. C* **2015**, *119* (16), 8786–8797.
- (3) Barskiy, D. A.; Knecht, S.; Yurkovskaya, A. V.; Ivanov, K. L. SABRE: Chemical Kinetics and Spin Dynamics of the Formation of Hyperpolarization. Progress in Nuclear Magnetic Resonance Spectroscopy. *Prog. Nucl. Magn. Reson. Spectrosc.* **2019**, 33–70.
- (4) Theis, T.; Ortiz, G. X.; Logan, A. W. J.; Claytor, K. E.; Feng, Y.; Huhn, W. P.; Blum, V.; Malcolmson, S. J.; Chekmenev, E. Y.; Wang, Q.; Warren, W. S. Direct and Cost-Efficient Hyperpolarization of Long-Lived Nuclear Spin States on Universal ¹⁵N₂-Diazirine Molecular Tags. *Sci. Adv.* **2016**, 2 (3), No. e1501438, DOI: 10.1126/sciadv.1501438.
- (5) Tomhon, P.; Abdulmojeed, M.; Adelabu, I.; Nantogma, S.; Shah, M.; Kabir, H.; Lehmkuhl, S.; Chekmenev, E. Y.; Theis, T. Temperature Cycling Enables Efficient 13 C SABRE-SHEATH Hyperpolar-Ization

- and Imaging of [1-13C]Pyruvate. J. Am. Chem. Soc. 2021, 282 DOI: 10.1021/jacs.1c09581.
- (6) Adelabu, I.; TomHon, P.; Kabir, M. S. H.; Nantogma, S.; Abdulmojeed, M.; Mandzhieva, I.; Ettedgui, J.; Swenson, R. E.; Krishna, M. C.; Theis, T.; Goodson, B. M.; Chekmenev, E. Y. Order-Unity 13C Nuclear Polarization of [1–13C]Pyruvate in Seconds and the Interplay of Water and SABRE Enhancement. *ChemPhysChem* **2022**, 23 (2), No. e202100839, DOI: 10.1002/cphc.202100839.
- (7) Wang, Z. J.; Ohliger, M. A.; Larson, P. E. Z.; Gordon, J. W.; Bok, R. A.; Slater, J.; Villanueva-Meyer, J. E.; Hess, C. P.; Kurhanewicz, J.; Vigneron, D. B. *Hyperpolarized ¹³C MRI: State of the Art and Future Directions. Radiology.* Radiological Society of North America Inc. May 1, 2019; pp 273–284. DOI: 10.1148/radiol.2019182391.
- (8) Gallagher, F. A.; Kettunen, M. I.; Hu, D. E.; Jensen, P. R.; Zandt, R. i. '.; Karlsson, M.; Gisselsson, A.; Nelson, S. K.; Witney, T. H.; Bohndiek, S. E.; Hansson, G.; Peitersen, T.; Lerche, M. H.; Brindle, K. M. Production of Hyperpolarized [1,4-¹³C₂]Malate from [1,4-¹³C₂]-Fumarate Is a Marker of Cell Necrosis and Treatment Response in Tumors. *Proc. Natl. Acad. Sci. U.S.A.* **2009**, *106* (47), 19801–19806.
- (9) Wilson, D. M.; Keshari, K. R.; Larson, P. E. Z.; Chen, A. P.; Hu, S.; Criekinge, M. V.; Bok, R.; Nelson, S. J.; Macdonald, J. M.; Vigneron, D. B.; Kurhanewicz, J. Multi-Compound Polarization by DNP Allows Simultaneous Assessment of Multiple Enzymatic Activities in Vivo. J. Magn. Reson. 2010, 205 (1), 141–147.
- (10) Nelson, S. J.; Kurhanewicz, J.; Vigneron, D. B.; Larson, P. E. Z.; Harzstark, A. L.; Ferrone, M.; van Criekinge, M.; Chang, J. W.; Bok, R.; Park, I.; Reed, G.; Carvajal, L.; Small, E. J.; Munster, P.; Weinberg, V. K.; Ardenkjaer-Larsen, J. H.; Chen, A. P.; Hurd, R. E.; Odegardstuen, L.-I.; Robb, F. J.; Tropp, J.; Murray, J. A. Metabolic Imaging of Patients with Prostate Cancer Using Hyperpolarized [1–13C]Pyruvate. *Sci. Transl Med.* **2013**, *5* (198), 198ra108.
- (11) Miloushev, V. Z.; Granlund, K. L.; Boltyanskiy, R.; Lyashchenko, S. K.; DeAngelis, L. M.; Mellinghoff, I. K.; Brennan, C. W.; Tabar, V.; Yang, T. J.; Holodny, A. I.; Sosa, R. E.; Guo, Y. W. W.; Chen, A. P.; Tropp, J.; Robb, F.; Keshari, K. R. Metabolic Imaging of the Human Brain with Hyperpolarized ¹³C Pyruvate Demonstrates 13C Lactate Production in Brain Tumor Patients. *Cancer Res.* **2018**, 78 (14), 3755–3760
- (12) Grist, J. T.; McLean, M. A.; Riemer, F.; Schulte, R. F.; Deen, S. S.; Zaccagna, F.; Woitek, R.; Daniels, C. J.; Kaggie, J. D.; Matys, T.; Patterson, I.; Slough, R.; Gill, A. B.; Chhabra, A.; Eichenberger, R.; Laurent, M. C.; Comment, A.; Gillard, J. H.; Coles, A. J.; Tyler, D. J.; Wilkinson, I.; Basu, B.; Lomas, D. J.; Graves, M. J.; Brindle, K. M.; Gallagher, F. A. Quantifying Normal Human Brain Metabolism Using Hyperpolarized [1– ¹³C]Pyruvate and Magnetic Resonance Imaging. *NeuroImage* **2019**, *189*, 171–179.
- (13) Gallagher, F. A.; Woitek, R.; McLean, M. A.; Gill, A. B.; Manzano Garcia, R.; Provenzano, E.; Riemer, F.; Kaggie, J.; Chhabra, A.; Ursprung, S.; Grist, J. T.; Daniels, C. J.; Zaccagna, F.; Laurent, M.-C.; Locke, M.; Hilborne, S.; Frary, A.; Torheim, T.; Boursnell, C.; Schiller, A.; Patterson, I.; Slough, R.; Carmo, B.; Kane, J.; Biggs, H.; Harrison, E.; Deen, S. S.; Patterson, A.; Lanz, T.; Kingsbury, Z.; Ross, M.; Basu, B.; Baird, R.; Lomas, D. J.; Sala, E.; Wason, J.; Rueda, O. M.; Chin, S.-F.; Wilkinson, I. B.; Graves, M. J.; Abraham, J. E.; Gilbert, F. J.; Caldas, C.; Brindle, K. M. Imaging Breast Cancer Using Hyperpolarized Carbon-13 MRI. *Proc. Natl. Acad. Sci. U. S. A.* **2020**, *117* (4), 2092–2098.
- (14) Kurhanewicz, J.; Vigneron, D. B.; Ardenkjaer-Larsen, J. H.; Bankson, J. A.; Brindle, K.; Cunningham, C. H.; Gallagher, F. A.; Keshari, K. R.; Kjaer, A.; Laustsen, C.; Mankoff, D. A.; Merritt, M. E.; Nelson, S. J.; Pauly, J. M.; Lee, P.; Ronen, S.; Tyler, D. J.; Rajan, S. S.; Spielman, D. M.; Wald, L.; Zhang, X.; Malloy, C. R.; Rizi, R. Hyperpolarized ¹³C MRI: Path to Clinical Translation in Oncology. Neoplasia (United States). *Neoplasia* 2019, 1–16, DOI: 10.1016/j.neo.2018.09.006.
- (15) Larson, P. E. Z.; Chen, H. Y.; Gordon, J. W.; Korn, N.; Maidens, J.; Arcak, M.; Tang, S.; Criekinge, M.; Carvajal, L.; Mammoli, D.; Bok, R.; Aggarwal, R.; Ferrone, M.; Slater, J. B.; Nelson, S. J.; Kurhanewicz, J.; Vigneron, D. B. Investigation of Analysis Methods for Hyper-

- polarized ¹³C-Pyruvate Metabolic MRI in Prostate Cancer Patients. *NMR Biomed* **2018**, *31* (11), No. e3997, DOI: 10.1002/nbm.3997.
- (16) Laustsen, C.; Østergaard, J. A.; Lauritzen, M. H.; Nørregaard, R.; Bowen, S.; Søgaard, L. V.; Flyvbjerg, A.; Pedersen, M.; Ardenkjaer-Larsen, J. H. Assessment of Early Diabetic Renal Changes with Hyperpolarized [1–¹³C]Pyruvate. *Diabetes Metab. Res. Rev.* **2013**, 29 (2), 125–129.
- (17) Lewis, A. J. M.; Tyler, D. J.; Rider, O. Clinical Cardiovascular Applications of Hyperpolarized Magnetic Resonance. *Cardiovasc Drugs Ther* **2020**, 34 (2), 231–240.
- (18) Grist, J. T.; Miller, J. J.; Zaccagna, F.; McLean, M. A.; Riemer, F.; Matys, T.; Tyler, D. J.; Laustsen, C.; Coles, A. J.; Gallagher, F. A. Hyperpolarized ¹³C MRI: A Novel Approach for Probing Cerebral Metabolism in Health and Neurological Disease. *J. Cerebral Blood Flow Metab.* **2020**, *1*, 1137–1147.
- (19) Browning, A.; Macculloch, K.; TomHon, P.; Mandzhieva, I.; Chekmenev, E. Y.; Goodson, B. M.; Lehmkuhl, S.; Theis, T. Spin Dynamics of $[1,2^{-13}C_2]$ Pyruvate Hyperpolarization by Parahydrogen in Reversible Exchange at Micro Tesla Fields. *Phys. Chem. Chem. Phys.* **2023**, 25 (24), 16446–16458.
- (20) Ohliger, M. A.; Grant, A. K.; Sodickson, D. K. Ultimate Intrinsic Signal-to-Noise Ratio for Parallel MRI: Electromagnetic Field Considerations. *Magn Reson Med.* **2003**, *50* (5), 1018–1030.
- (21) Wang, J.; Kreis, F.; Wright, A. J.; Hesketh, R. L.; Levitt, M. H.; Brindle, K. M. Dynamic 1H Imaging of Hyperpolarized [1–¹³C]Lactate in Vivo Using a Reverse INEPT Experiment. *Magn Reson Med.* **2018**, 79 (2), 741–747.
- (22) Mandzhieva, I.; Adelabu, I.; Chekmenev, E. Y.; Theis, T. Proton-Only Sensing of Hyperpolarized $[1,2^{-13}C_2]$ Pyruvate. ACS Sens 2022. 73773.
- (23) Iali, W.; Roy, S. S.; Tickner, B. J.; Ahwal, F.; Kennerley, A. J.; Duckett, S. B. Hyperpolarising Pyruvate through Signal Amplification by Reversible Exchange (SABRE). *Angewandte Chemie International Edition* **2019**, 58 (30), 10271–10275.
- (24) Tickner, B. J.; Semenova, O.; Iali, W.; Rayner, P. J.; Whitwood, A. C.; Duckett, S. B. Optimisation of Pyruvate Hyperpolarisation Using SABRE by Tuning the Active Magnetisation Transfer Catalyst. *Catal. Sci. Technol.* **2020**, *10* (5), 1343–1355.
- (25) Schmidt, A. B.; De Maissin, H.; Adelabu, I.; Nantogma, S.; Ettedgui, J.; Tomhon, P.; Goodson, B. M.; Theis, T.; Chekmenev, E. Y. Catalyst-Free Aqueous Hyperpolarized [1–¹³C]Pyruvate Obtained by Re-Dissolution Signal Amplification by Reversible Exchange. *ACS Sens* **2022**, *7* (11), 3430–3439.
- (26) Browning, A.; Mcculloch, K.; Bedoya, D. G.; Dedesma, C.; Goodson, B. M.; Rosen, M. S.; Chekmenev, E. Y.; Yen, Y.-F.; Tomhon, P.; Theis, T. Facile Hyperpolarization Chemistry for Molecular Imaging and Metabolic Tracking of [1–13C]Pyruvate in Vivo. *ChemPhysChem* 2023, DOI: 10.26434/chemrxiv-2023-4dqkx.
- (27) De Maissin, H.; Groß, P. R.; Mohiuddin, O.; Weigt, M.; Nagel, L.; Herzog, M.; Wang, Z.; Willing, R.; Reichardt, W.; Pichotka, M.; Heß, L.; Reinheckel, T.; Jessen, H. J.; Zeiser, R.; Bock, M.; Von Elverfeldt, Dominik; Zaitsev, M.; Korchak, S.; Glöggler, S.; Hövener, J.-B.; Chekmenev, E. Y.; Schilling, F.; Knecht, S.; Schmidt, A. B. In Vivo Metabolic Imaging of [1–13C]Pyruvate-D₃ Hyperpolarized By Reversible Exchange With Parahydrogen. 2023 DOI: 10.26434/chemrxiv-2023-9trxb.
- (28) Datta, K.; Spielman, D. MRI of [2-13C]Lactate without *J*-Coupling Artifacts. *Magn Reson Med.* **2021**, 85 (3), 1522–1539.
- (29) Coffey, A. M.; Shchepin, R. V.; Truong, M. L.; Wilkens, K.; Pham, W.; Chekmenev, E. Y. Open-Source Automated Parahydrogen Hyperpolarizer for Molecular Imaging Using ¹³C Metabolic Contrast Agents. *Anal. Chem.* **2016**, 88 (16), 8279–8288.
- (30) Theis, T.; Truong, M. L.; Coffey, A. M.; Shchepin, R. v.; Waddell, K. W.; Shi, F.; Goodson, B. M.; Warren, W. S.; Chekmenev, E. Y. Microtesla SABRE Enables 10% Nitrogen-15 Nuclear Spin Polarization. J. Am. Chem. Soc. 2015, 137 (4), 1404–1407.
- (31) Viale, A.; Reineri, F.; Santelia, D.; Cerutti, E.; Ellena, S.; Gobetto, R.; Aime, S. Hyperpolarized agents for advanced MRI investigations. *Q. J. Nucl. Med. Mol. Imaging* **2009**, 53 (6), 604–617.

- (32) Daniels, C. J.; Mclean, M. A.; Schulte, R. F.; Robb, F. J.; Gill, A. B.; Mcglashan, N.; Graves, M. J.; Schwaiger, M.; Lomas, D. J.; Brindle, K. M.; Gallagher, F. A. A Comparison of Quantitative Methods for Clinical Imaging with Hyperpolarized ¹³C-Pyruvate. *NMR Biomed* **2016**, 29 (4), 387–399.
- (33) Hu, S.; Larson, P. E. Z.; VanCriekinge, M.; Leach, A. M.; Park, I.; Leon, C.; Zhou, J.; Shin, P. J.; Reed, G.; Keselman, P.; Von Morze, C.; Yoshihara, H.; Bok, R. A.; Nelson, S. J.; Kurhanewicz, J.; Vigneron, D. B. Rapid Sequential Injections of Hyperpolarized [1–13C]Pyruvate in Vivo Using a Sub-Kelvin. *Multi-Sample DNP Polarizer. Magn Reson Imaging* **2013**, 31 (4), 490–496.
- (34) Nelson, S. J.; Vigneron, D.; Kurhanewicz, J.; Chen, A.; Bok, R.; Hurd, R. DNP-Hyperpolarized 13C Magnetic Resonance Metabolic Imaging for Cancer Applications. *Appl. Magn. Reson.* **2008**, *34* (3–4), 533–544.
- (35) Vazquez-Serrano, L. D.; Owens, B. T.; Buriak, J. M. The Search for New Hydrogenation Catalyst Motifs Based on N-Heterocyclic Carbene Ligands. *Inorg. Chim. Acta* **2006**, 359 (9), 2786–2797.
- (36) Cowley, M. J.; Adams, R. W.; Atkinson, K. D.; Cockett, M. C. R.; Duckett, S. B.; Green, G. G. R.; Lohman, J. A. B.; Kerssebaum, R.; Kilgour, D.; Mewis, R. E. Iridium N-Heterocyclic Carbene Complexes as Efficient Catalysts for Magnetization Transfer from Para-Hydrogen. *J. Am. Chem. Soc.* **2011**, *133* (16), 6134–6137.
- (37) Barskiy, D. A.; Kovtunov, K. V.; Koptyug, I. V.; He, P.; Groome, K. A.; Best, Q. A.; Shi, F.; Goodson, B. M.; Shchepin, R. V.; Coffey, A. M.; Waddell, K. W.; Chekmenev, E. Y. The Feasibility of Formation and Kinetics of NMR Signal Amplification by Reversible Exchange (SABRE) at High Magnetic Field (9.4 T). *J. Am. Chem. Soc.* **2014**, 136 (9), 3322–3325.
- (38) Waddell, K. W.; Coffey, A. M.; Chekmenev, E. Y. In Situ Detection of PHIP at 48 mT: Demonstration Using a Centrally Controlled Polarizer. *J. Am. Chem. Soc.* **2011**, *133* (1), 97–101.
- (39) Nantogma, S.; Eriksson, S. L.; Adelabu, I.; Mandzhieva, I.; Browning, A.; TomHon, P.; Warren, W. S.; Theis, T.; Goodson, B. M.; Chekmenev, E. Y. Interplay of Near-Zero-Field Dephasing, Rephasing, and Relaxation Dynamics and [1–13C]Pyruvate Polarization Transfer Efficiency in Pulsed SABRE-SHEATH. *J. Phys. Chem. A* **2022**, *126* (48), 9114–9123.
- (40) Nantogma, S.; Joalland, B.; Wilkens, K.; Chekmenev, E. Y. Clinical-Scale Production of Nearly Pure (>98.5%) Parahydrogen and Quantification by Benchtop NMR Spectroscopy. *Anal. Chem.* **2021**. 933594.
- (41) Joalland, B.; Nantogma, S.; Chowdhury, M. R. H.; Nikolaou, P.; Chekmenev, E. Y. Magnetic Shielding of Parahydrogen Hyperpolarization Experiments for the Masses. *Magn. Reson. Chem.* **2021**, 59 (12), 1180–1186.
- (42) Joalland, B.; Nantogma, S.; Chowdhury, M. R. H.; Nikolaou, P.; Chekmenev, E. Y. Magnetic Shielding of Parahydrogen Hyperpolarization Experiments for the Masses. *Magn. Reson. Chem.* **2021**, 59 (12), 1180–1186.
- (43) Coffey, A. M.; Truong, M. L.; Chekmenev, E. Y. Low-Field MRI Can Be More Sensitive than High-Field MRI. *J. Magn. Reson.* **2013**, 237, 169–174
- (44) Laustsen, C.; Pileio, G.; Tayler, M. C. D.; Brown, L. J.; Brown, R. C. D.; Levitt, M. H.; Ardenkjaer-Larsen, J. H. Hyperpolarized Singlet NMR on a Small Animal Imaging System. *Magn Reson Med.* **2012**, *68* (4), 1262–1265.
- (45) Feng, Y.; Theis, T.; Wu, T. L.; Claytor, K.; Warren, W. S. Long-Lived Polarization Protected by Symmetry. *J. Chem. Phys.* **2014**, *141*, 134307.
- (46) Pileio, G.; Carravetta, M.; Levitt, M. H. Storage of Nuclear Magnetization as Long-Lived Singlet Order in Low Magnetic Field. *Proc. Natl. Acad. Sci. U. S. A.* **2010**, *107* (40), *17135–17139*.
- (47) Eills, J. Advances in Parahydrogen-Enhanced Nuclear Magnetic Resonance; Doctoral Thesis, 2019.
- (48) Tayler, M. C. D.; Theis, T.; Sjolander, T. F.; Blanchard, J. W.; Kentner, A.; Pustelny, S.; Pines, A.; Budker, D. Instrumentation for Nuclear Magnetic Resonance in Zero and Ultralow Magnetic Field. *Rev. Sci. Instrum.* **2017**, *88*, 091101.

- (49) Sabba, M.; Wili, N.; Bengs, C.; Brown, L. J.; Levitt, M. H. Symmetry-Based Singlet-Triplet Excitation in Solution Nuclear Magnetic Resonance. *J. Chem. Phys.* **2022**, *157*, 134302.
- (50) Schwartz, I.; Scheuer, J.; Tratzmiller, B.; Müller, S.; Chen, Q.; Dhand, I.; Wang, Z.-Y.; Müller, C.; Naydenov, B.; Jelezko, F.; Plenio, M. B. Robust Optical Polarization of Nuclear Spin Baths Using Hamiltonian Engineering of Nitrogen-Vacancy Center Quantum Dynamics. Sci. Adv. 2018, No. eaat8978, DOI: 10.1126/sciadv.aat8978.
- (51) Tratzmiller, B. Pulsed Control Methods with Applications to Nuclear Hyperpolarization and Nanoscale NMR. *Diss. Universität Ulm* **2021**, DOI: 10.18725/OPARU-39283.
- (52) DeVience, S. J.; Greer, M.; Mandal, S.; Rosen Stephen, J.; DeVience, M. S.; Rosen, M. S. Homonuclear J-Coupling Spectroscopy at Low Magnetic Fields Using Spin-Lock Induced Crossing. *ChemPhysChem* **2021**, 22 (20), 2128.
- (53) DeVience, S. J.; Greer, M.; Mandal, S.; Rosen, M. S. Homonuclear J-Coupling Spectroscopy at Low Magnetic Fields Using Spin-Lock Induced Crossing**. *ChemPhysChem* **2021**, 22 (20), 2128–2137.
- (54) Hogben, H. J.; Krzystyniak, M.; Charnock, G. T. P.; Hore, P. J.; Kuprov, I. Spinach A Software Library for Simulation of Spin Dynamics in Large Spin Systems. *J. Magn. Reson.* **2011**, 208 (2), 179–194.
- (55) Feng, Y.; Davis, R. M.; Warren, W. S. Accessing Long-Lived Nuclear Singlet States between Chemically Equivalent Spins without Breaking Symmetry. *Nat. Phys.* **2012**, *8* (11), 831–837.
- (56) Viale, A.; Reineri, F.; Santelia, D.; Cerutti, E.; Ellena, S.; Gobetto, R.; Aime, S. Hyperpolarized Agents for Advanced MRI Investigations. Q. J. Nucl. Med. Mol. Imaging 2009, 53 (6), 604–617.